EUROPEAN ORGANIZATION FOR NUCLEAR RESEARCH

CERN–PPE/95–104
16 June 1995

SCINTILLATING FIBRES

Heinrich Leutz

CERN, Geneva, Switzerland

Abstract

This review first describes the basic working principles of scintillating fibres together with their most common readout techniques. It concentrates on plastic fibres, since they are better suited for application in High Energy Physics. The following section reviews fibre trackers and lead/scintillating calorimeters. Both detector devices are compared with competing techniques based on other media. The review continues with dose rates at the LHC-collider and discusses the radiation damage on scintillating fibres. The conclusion covers the progress achieved with the fibre technique and presents an outlook on future developments.

Submitted to Nucl. Instr. and Methods

I INTRODUCTION

Particle detection with scintillating organic or inorganic solids and liquids has been refined during the last decade by the fibre technique, where scintillating cores with diameters ranging from several micrometres up to a few millimetres are surrounded by a cladding layer (≥ 5 μm) of lower refractive index. This structure is called “step-index” fibre in contrast to the “gradient-index fibre”, (not used for scintillating fibres), where the refractive index decreases smoothly from the fibre axis to its surface. The step-index fibre traps by total reflections on its core-cladding interface a small fraction of the scintillation light, induced by ionization losses, and guides it via total reflections to the fibre end. There, it is detected by the photocathode of a photomultiplier or of an image intensifier. Scintillating fibres should not be confused with clear optical fibres, which are not doped with scintillators and are principally used to transport optical communications over long distances.

The detection of ionizing radiation with scintillating material has been quite generally practiced in the past, first in nuclear physics and subsequently in particle physics. Early attempts for improved granularity were reported during the late fifties, in which unclad plastic filaments were used [1-4]. These first fibre approaches became obsolete, since bubble- and spark chambers were the most frequently applied techniques for particle tracking at that time. In particular bubble chamber techniques offered better track quality and spatial resolution. Chambers filled with liquid hydrogen provided ideal proton targets with long radiation- and interaction lengths. Scintillating fibre techniques became interesting again in the early eighties, with the advent of particle colliders and the necessity to detect rare particles in the presence of high background rates. Short light decay times of scintillators allowed high data acquisition rates and the mechanical properties of fibres permitted them to follow the required geometries of 4π-detectors. In addition, considerable advances in the technologies associated with the fibre technique have been achieved since the late fifties, e.g., multi-anode photomultipliers, image intensifiers, and CCD-cameras of high performance.

Since the early eighties, two main kinds of scintillating fibres have been used in parallel : glass fibres and plastic ones. In 1981, Borenstein et. al. [5] reported on the properties of plastic fibres, with light decay times of a few nanoseconds, followed by Allemand et. al. [6] and Blumenfeld et. al. [7] in 1984. D.M. Potter [8] initiated in 1981 the application of glass fibres. In 1983, terbiumoxide doped glass fibres with 25 μm diameter were assembled by Ruchti et. al. [9] to a 4 mm thick target plate, which was viewed by a three stage image intensifier. Three years later, A. Bross [10] applied multi glass fibres doped with ceriumoxide. They were of square cross-sections (25 μm edges) and formed a square bundle of 0.5 mm edges. Their light decay time was about 120 ns, a definite advantage compared to the 10 ms of the terbium doped ones.

Scintillating fibres are produced nowadays either from glasses, or from plastic polymers, e.g. polystyrene (PS) for the core (table 1) and polymethylmethacrylate (PMMA) for the cladding. Instead of solid fibres, also glass capillaries, which serve as cladding, can be filled with scintillating liquids of higher refractive index [11-13]. As compared with glass-fibres [14] (table 2), plastic ones and scintillating liquids in capillaries, which have similar properties, have better photon yield, longer light attenuation [15], shorter scintillation decay times [16, 17] and longer nuclear interaction-and radiation lengths, all of which make them more suitable for detector applications.

Therefore, this article is mainly concerned with plastic fibres and it starts with Basic Principles, including working conditions of scintillating fibres, the scintillation process and photoelectron counting. Then, it continues with a section on the Detection of Fibre Scintillations, which treats photocathodes, position sensitive photomultipliers, visible light photon counters, phosphor screens, spatial resolution of optoelectronic chains, proximity focussed image intensifiers, micro-channel plates, charged coupled devices and imaging with silicon pixel arrays (ISPA).

The main applications of scintillating fibres in High Energy Physics are in particle tracking with fibre diameters well below 1 mm, and in calorimetry with diameters of 1 mm and above. Therefore, the last chapter on Scintillating Fibres in High Energy Physics is structured in the following way : particle tracking (the UA2 fibre tracker, the Chorus fibre tracker, the proposed fine grain central tracker) and calorimetry with scintillating fibres.

The chapter on High Energy Physics Applications ends with a paragraph on dose rates and radiation damage for Fibre Detectors at LHC. It quotes dose rates for fibre trackers with different distances of fibre shells from the collider axis and discusses the main parameters, which could influence the radiation damage of plastic fibres. Finally, the conclusions review the progress achieved with the scintillating fibre technique within the last few years and present an outlook on future developments.

II BASIC PRINCIPLES

Working Conditions of Scintillating Fibres

The PS-core is clad with PMMA of lower refractive index ($n_{clad} < n_{ps}$) and the fibre traps a fraction t of the scintillating light contained within its total reflection cones (fig. 1). The cladding also protects the fibre core against deterioration of its surface, which otherwise would result in bad total reflection conditions. For meridional light rays[#1] the trapping fraction amounts to :

[#1] Skew light rays arise mostly at the rim of the fibre core and spiral along the core-cladding interface. Adding them to meridional rays would change relation (1) to $t' = 1-(n_2/n_1)^2$. They

$$t = 1 - (n_2 / n_1) \qquad (1)$$

where n_1 refers to the PS core and n_2 to the acrylic cladding.

The untrapped light fraction n_2 / n_1 is absorbed by an extra mural absorber (EMA) if the fibre is coated with a black layer. Even if the EMA is not present, the untrapped light fraction escapes at an angle, which prevents it from being retrapped in a neighbouring fibre and disappears after some 50 mm of fibre length without causing noticeable cross-talk.

The trapped light fraction is guided via N subsequent total reflections (critical angle α, $\sin \alpha = n_2 / n_1$) to the fibre end :

$$N = \cot \alpha \; L/d \qquad (2)$$

with L meaning the fibre length and d its diameter. The numerical aperture NA of the fibre is again defined by the respective refractive indices :

$$NA = (n_1^2 - n_2^2)^{1/2} = \sin\theta \qquad \text{(fig. 1)} \qquad (3)$$

The fibre diameter defines the spatial resolution and, for tracking detectors, we are interested in keeping it small. A decrease in fibre diameter is counterbalanced by the increasing number N of reflections (relation 2). Since imperfections at the fibres' core-cladding interfaces, cause small reductions from unity for the total reflection coefficient q, the increased number of reflections induces light losses ($I/I_0 = q^N$) and we obtain as an approximation [15] the reflection length Λ_R(m), which indicates the distance l, where the injected light intensity $I / I_i = e^{-l/\Lambda_R}$ is reduced to 1 / e due to these reflection losses

$$\Lambda_R = \frac{d}{1 - q \;\; NA^2} \qquad (4)$$

Therefore, with small fibre diameters d[m], the reflection losses, which have been measured for Kuraray fibres [15], contribute noticeably together with the absorption length Λ_A ($I_A/I = 1/e$) and the scattering length Λ_{Sc} ($I_{Sc}/I = 1/e$) to the total fibre attenuation length Λ:

$$\Lambda^{-1} = \Lambda_A^{-1} + \Lambda_R^{-1} + \Lambda_{Sc}^{-1} \qquad (5)$$

The absorption length Λ_A [m] is mainly caused by the decadic molar extinction coefficient ε_λ [l/m·mole] of the fibre dopant within the dopant's emission band (fig. 3), and is defined as the value of the light pathlength D[m] at which the light yield Y(D) drops to 1/e of its initial value at zero D :

---

suffer much more total reflections than meridional ones and are diffused out of the core after short travelling paths compared to meridional rays.

$$Y(D) = \int_{em} I_{\lambda}^{em} \; 10^{-\varepsilon_{\lambda} CD} \; d\lambda \qquad (6)$$

with I_{λ}^{em} meaning the emission intensity normalized to unity and C the scintillator concentration [mole / l]. It is therefore important to use scintillators where the absorption- and emission maxima are well separated, i.e. with large Stokes' shifts.

The scattering length Λ_{sc} [m] quantifies Rayleigh scattering on small density fluctuations in the PS core. Fig. 2 shows the attenuation lengths mainly caused by light scattering for light injected parallel to the axis of an undoped PS-fibre. They contribute noticeably to the total light attenuation below 400 nm and drop to 0.03 m at 340 nm, the p-terphenyl emission maximum (table3). This behaviour explains the opacity of polystyrene although its absorption band peaks at 265 nm (table 1), far from the p-terphenyl emission.

The Scintillation Process

The energy lost by an ionizing particle first excites the electronic (rotational and vibrational) levels of PS (fig. 3a). Since the PS-fluorescence yield is rather poor (table 1), it must be enhanced by adding an aromatic scintillator. The intermolecular energy transfer[#2] between the respective quantum levels requires that the PS-emission band overlap the scintillator absorption band. If the added scintillator emits in the opaque region of PS (see fig. 2), e.g. p - terphenyl (fig. 3b), a wavelength shifter (fig. 3c) is needed to shift its light emission into the transparent region of PS (2-component system), where Rayleigh scattering becomes unimportant and the PS-attenuation length reaches about 2.4 m (fig. 2).

A sufficiently high scintillator concentration (above 0.015 molar fraction) provides mainly non radiative and therefore local energy transfer (Förster transitions) [18] between the PS- and the scintillator. This comparatively high concentration can be added with PMP (1-phenyl–3-mesityl–2-pyrazoline) [19], since due to its large Stokes' shift (table3) it emits in the transparent PS-region (1-component system) and the long wavelength tail of its absorption band (fig. 3d) causes only small self-absorptions within its emission band. This is not the case with a 2-component system, since absorption and emission of POPOP and other wavelength shifters (table3) overlap within a large wavelength region (fig. 3c). This overlap must be compensated by a much lower POPOP-concentration and its molecules are therefore too distant to enable non-radiative Förster-transitions. This is obvious from fig. 4 which shows the self absorption of POPOP- and PMP 420-solutions in toluene caused by different

---

[#2] A historical development of theories on the excitation of electronic states and the intermolecular energy transfer can be found in the books of I. B. Berlman : "Handbook of Fluorescence spectra of aromatic molecules", Academic Press, New York and London (1971) and "Energy Transfer Parameters of Aromatic Compounds"; same publisher (1973).

absorption lengths. The respective absorption bands were excited with light from a double-monochromator and the emssion was analysed by a single-monochromator [20]. In spite of a POPOP concentration (0.0025 molar fraction) ten times smaller than that for PMP-420 (0.025 molar fraction), the POPOP self-absorption is still much more pronounced due to its large overlap.

Therefore, with a 2-component system, normal radiative exchange of light emission and reabsorption takes place between the two dopants which requires optical absorption lengths longer than 150 µm. Consequently the light emitted from the first dopant can escape from fibres of small diameters , excite the wavelength shifter in neighbour fibres and cause unwanted cross-talk. This is particularly true for bundles of PS-fibres, since it is not possible to produce them with extra mural absorbers. Cross-talk can be avoided by doping the PS matrix with only one scintillator (1-component system) having a large Stokes shift and therefore small overlap between its absorption and emission bands, e.g. PMP or 3HF (3-hydroxyflavone) [21]. At appropriate concentrations, they produce local Förster-transitions between the relevant PS-and their proper energy levels. 3HF has practically zero overlap but yields only about 40% emission as compared with PMP (table3).

This is demonstrated in fig. 5. Two fibre bundles of 1 mm diameter containing 30 µm diameter individual fibres have been excited with a Nd-YAG laser at 265 nm wavelength. The emitted light, guided through 150 mm bundle length, was photographed with a CCD camera [22]. The left-hand photograph shows the result obtained from the fibres doped with p-terphenyl and the POPOP-wavelength shifter. It indicates cross-talk over six fibre-layers. In contrast, the right-hand photograph displays the picture taken with the PMP-doped fibre bundle, where light is emitted and guided only from the first fibre-layer exposed to the laser beam. Since no light is lost via cross-talk, the light yield from this layer is much higher than on the left hand photograph.

Photoelectron Counting with Scintillating Fibres

Photoelectron counting characterizes quality and performance of scintillating fibres in an objective way in contrast to the often quoted attenuation lengths. Attenuation lengths are composed of different attenuation terms (relation 5) and their attenuation plots deviate therefore from straight lines in logarithmic representations. Therefore, they depend on the fibre lengths between which they are quoted. Until recently, most photoelectron counting procedures were based on photomultipliers, where the Quantacon[#3] resolved up to three photoelectron peaks [23]. Since 1992 an electrostatically focused hybrid photomultiplier tube (HPMT)[#4] has been commercially available, which contains a silicon diode bombarded with electrons from a light detecting photocathode (fig. 6). With 13 kV potential difference, it results in an average

---

[#3] 8850, Burle Electron Tubes, Lancaster, PA, USA

[#4] BV Delft Elektronische Producten (DEP) NL-9300 A B Roden, The Netherlands

of 3575 electron-hole pairs per photoelectron and exceeds by more than two orders of magnitude the electron multiplication at the first dynode of a photomultiplier. This is reflected in the statistical fluctuations and increases the number of resolved photoelectron peaks to about fifteen [24].

Photoelectron yields were measured [25] on fused fibre bundles [26] containing 1600 fibres of 60 µm diameter within squared cross-sections of 2.5 mm edges[#5] (fig. 7). Each individual fibre (fig. 8) shares its double cladding [23, 25], which consists of standard polymethyl-methacrylate of 1.49 refractive index and fluorinated polymethacrylate of 1.42 refractive index, with its next neighbours.

Typical measured photoelectron spectra are displayed in fig. 9 for different source positions. They show discrete gaussian peaks on top of a continuum, caused by backscattering of photoelectrons from the HPMT-diode. The number b of backscattered electrons follows a Poisson distribution :

$$P(b) = \frac{(<n>\ \alpha)^b}{b!}\ e^{-\alpha<n>} \qquad (7)$$

with P(b) being the probability of having b backscattered photoelectrons. The measured backscattered fraction α agrees with ref. [27] and completely explains [24] the spectral shapes in fig. 9.

Hit densities measured with a Quantacon for 1 mm monofibres from different suppliers are listed in table 4. The Bicron fibre (99-02) showed the outstandingly small light attenuation with distance of only 3.3 times between zero position and 2 m.

Four fibre bundles were more recently measured with the HPMT [25] and these results are listed in table 5. The improvement in hit densities is mainly due to the fluorinated polymethacrylate cladding, which increases, with its 1.42 refractive index, the trapping fraction by 1.75 times. Additional improvement is due to the better photoelectron collection efficiency of the HPMT as compared to that of the first Quantacon dynode.

III DETECTION OF FIBRE SCINTILLATIONS

Photocathodes

Photocathodes can be manufactured from a variety of compounds and each type has its characteristic spectral response : S11 (Sb-Cs), Bialkali (Sb-K-Cs or Sb-Rb-Cs), S20 (Na-K-Sb-Cs) Trialkali , S1 (Ag-O-Cs) and others. Their spectral response is measured as radiant sensitivity $R(\lambda)$ (photocathode current emitted per watt of incident radiation at wavelength λ) or as quantum efficiency $QE(\lambda)$:

[#5] Kuraray Co. Ltd. Tokyo, Japan

$$QE(\lambda) = \frac{R(\lambda) \times 1.24}{\lambda} \qquad (8)$$

where $R(\lambda)$ is in mA W^{-1}, the wavelength λ in nm, and 1.24 is the conversion factor from wavelength to photon energy. For example, a quantum efficiency of 0.25 at 400 nm wavelength is equivalent to a radiant sensitivity of 80.6 mA/W.

Photocathodes are evaporated as thin films on the inside of the tube's light input window. To preserve the spatial resolution of the attached scintillating fibres, this window is made from a stack of fused clad glass fibres (ø 5 µm to 20 µm). The light transmission of optical fibre windows depends on their numerical aperture (NA_{fibre} ² NA_{window}), packing fraction (related to the fibre diameter) and the absorption characteristics of the fibre cores.

Position Sensitive Photomultipliers (PSPM)

The photon image of scintillating fibres hitting the photocathode is conserved through the electron multiplication at the dynode stages and is reproduced in the multianode plane. Losses in spatial resolution are mainly due to the spread of secondary electrons at the dynodes. This drawback is counterbalanced by high gain and by fast response (a few nanoseconds). The anode plane consists either of crossed wires (up to 16×16) or arrays of up to 256 anodes with about 3 mm pitch. Aligned with a solenoidal field, cross-talk between anode wires or pixels is reduced and the spatial resolution improved but the gain of one million at zero magnetic flux density drops to some ten thousands at 1 T. Several types of PSPMs are offered by principally two manufacturers[#6].

Visible Light Photon Counters (VLPC)

VLPCs are silicon solid-state photomultipliers [28] with optimized response in the visible light region. A visible photon is either absorbed in the undoped blocking layer or in the doped gain region. From the blocking layer the electron is collected at the top contact and the hole drifts into the gain region, where it produces free electrons by impact ionization with neutral donor (As) impurities. The impurity concentration is high enough to form an energy band separated from the silicon conduction band by 0.05 eV ionization energy. The photon absorbed in the gain region produces almost the same electron avalanche as the hole from the blocking layer if the electric field is approximately 1 kV cm^{-1}. The avalanche is limited to some 10^4 electrons because of electron-hole recombinations.

With antireflective coating the VLPC quantum efficiency reaches about 85% at 550 nm. In order to reduce intolerably high thermal noise, the VLPCs need to be

---

[#6] Hamamatsu Photonics K.K., Toyooka-village, Japan
Philips Photonics, with offices in USA, U.K., France, Germany, Japan

cryogenically cooled to an optimum operating temperature T of 6.5 K. Below this temperature ($\Delta T = -0.1$ K) the avalanche gain is reduced and above ($\Delta T = +0.1$ K), the signal-to-noise ratio worsens rapidly. Fig. 10 shows three photoelectron spectra taken of a Sr-90 β-source positioned at different distances. They should be compared with those shown in fig. 9, which were taken with an HPMT-tube and clearly show better signal-to-noise ratios. VLPCs can be attached to individual fibres only, which limits the tracker's granularity. In contrast, detectors converting scintillations into electrons via photocathodes are not limited in fibre sizes since the photolayers with less than 3 µm granularity match fibres down to 10 µm diameter.

Phosphor Screens

Phosphors are highly purified inorganic crystalline materials to which small amounts of dopants have been added. They convert electron energy into radiant energy. Their crystals are sized between 0.2 and 20 micrometres and are photo- or vapour deposited on glass substrates at the output optical fibre windows of image intensifiers. For conversions of fibre images in a optoelectronic chain, they must be fast, of high spatial resolution and their light emission must be matched with the subsequent photocathode- or CCD-sensitivity. Some typical phosphors used for image intensifiers are listed in table 6.

The Spatial Resolution of Opto-Electronic Chains

In this context, we should clearly distinguish between spatial precision, which means the accuracy to locate a hit within the detector's frame, and spatial resolution. This latter term is defined as the classical resolving power in optics : two neighboured objects are resolved if the principal maxima of their diffraction patterns (Airy discs) are just separated. This is mathematically defined with the Modulation Transfer Function (MTF), which for circular apertures and far field has the form :

$$\mathrm{MTF} = 2/\pi \left[\arccos(\omega/2) - \omega\left(1-\omega^2/4\right)^{1/2} \right] \qquad (9)$$

with $\omega = (f\ \lambda\ l)/(\pi\ \rho)$, where f (line pairs/mm) means the spatial frequency, ρ (mm) the diameter of the aperture, λ (mm) the wavelength and l (mm) the distance between aperture and image plane. The MTF varies between unity (complete separation of the Airy discs) and zero (complete overlap) : $0 \le \omega \le 2$.

For a scintillating fibre bundle directly attached to a detecting photocathode, the MTF becomes :

$$\mathrm{MTF} = \left(\frac{2\ J_1(d\ f)}{\pi\ d\ f} \right)^2 \qquad (10)$$

with J_1 being the Bessel function of the first kind and d (mm) the fibre diameter.

In an opto-electronic chain, consisting of scintillating fibres, fibre optics windows, image intensifiers, scintillation screens, etc, the total MTF_{tot} is given by the product of the individual components MTF_i :

$$MTF_{tot} = \prod_i (MTF)_i \qquad (11)$$

Accordingly, the number f_{tot} of line pairs per mm of an opto-electronic chain is composed of the individual spatial frequencies f_i, and their reciprocal values add quadratically :

$$f_{tot}^{-2} = \sum_i f_i^{-2} \qquad (12)$$

In most cases, the spatial frequencies of image intensifiers, fibre optics windows, and other optical components are quoted as the limiting resolution for MTF = 0.03.

Proximity-focussed Image Intensifiers

These devices achieve distortion-free image conversions between photocathode and phosphor screen which are in close proximity (between 3 mm and 5 mm) to each other (fig. 11). Their gain of about 50 W/W is due to their high potential difference of 25 kV.

Their limiting resolution is about 40 line pairs / mm. Proximity focussed intensifiers immediately follow the fibre end faces. Depending on the desired amplification one might use a chain of up to three intensifiers followed in many arrangements by MCPs and CCDs.

Micro-Channel Plate Image Intensifiers (MCP)

These tubes yield large photoelectron multiplications, which are achieved with micro-channel plates, located inside the tube between photocathode and phosphor screen (fig. 12). A microchannel plate is a 0.5 to 1 mm thick disc, which contains closely packed 6 µm to 15 µm thin hollow tubes, across which a potential difference of several hundred Volts is applied. The electrons, emitted from the opposite cathode, are accelerated by a 200 V potential difference and enter the MCP, where electron multiplication is produced via successive interactions with the walls of the hollow tubes. Electrons leaving the MCP are finally accelerated to the phosphor screen by a potential difference of approximately 10 kV.

A drawback of MCPs is the packing fraction of the hollow tubes, which worsens the spatial resolution and reduces the original hit density of scintillating fibres. In addition, moderate magnetic flux densities (^{3} 0.5 T), prevent the electrons from hitting the tube walls and therefore stop electron multiplication.

Charged Coupled Devices (CCD)

CCDs convert optical images (in most cases from phosphor screens of image intensifiers), into electronic signals. This is achieved by an array of photoelements (silicon pixels) of some tens of micrometres edge dimensions arranged in a two dimensional matrix of about $1\,cm^2$ area (image zone). Each pixel stores the photocharges in a MOS capacitor (space charge zone) and transfers them sequentially as an analog shift register to a memory zone, which is masked from incident light. The charges are finally accumulated in the readout register, and a diode converts the electric charges into voltage signals. These operations are driven by a clock in the megahertz frequency range and the entire readout process for a CCD-array takes a few milliseconds. In most cases, each pixel is protected against over-illumination (antiblooming), by a diode, which is separated from the photoelement by a potential barrier. The excess charges are drained off as a weak current.

A thinned CCD matrix yields electronic signals if bombarded with electrons at its rear face (EB-CCD). The electrons hit the pixels on their rear side, which is thinned to allow their penetration into the space charge zone. In this way, photoelectrons emitted from photocathodes can be directly detected by the CCD-matrix without the intermediate stage of a phosphor screen. Drawbacks are their readout times of several milliseconds and their noise sources, which necessitate additional light amplification with an image intensifier to achieve satisfactory signal/noise ratios.

Imaging with Silicon Pixel Arrays (ISPA)

A new development for photon counting and imaging of low intensity light patterns, in particular from scintillating fibres, is the use of hybrid photomultiplier tubes (HPMT) or imaging silicon pixel arrays (ISPA) directly bombarded with electrons emitted from light detecting photocathodes. The principle of HPMTs has been known since the sixties [30-37] and has been further developed in recent years. [24, 38]. Photon counting with HPMTs has already been realized [25] and is described earlier in this article.

Replacing the silicon diode by an avalanche photodiode (APD) results in a hybrid avalanche photodiode (HAPD) with intrinsic APD-gain. Unfortunately, as reported by several authors [39-41], APDs fail abruptly when operated in the presence of particles, even well below their maximum gain.

Ongoing developments [42-44] are currently emphasizing the replacement of phosphor screens of customary image intensifiers by silicon pixel anodes, mounted inside a phototube (fig. 13) and digitally readout in a line-parallel mode (fig. 14). This solution improves the electron multiplication, shortens the readout time, and allows one ISPA-

stage to achieve better spatial resolution (see relation 12) than with the normally adopted bulky optoelectronic chain of several image intensifiers. Spatial resolution of photoelectrons is conserved by either proximity arrangement of photocathode and pixel matrix (replacing the phosphor screen in fig. 11), or by electrostatic or magnetic focussing. In the latter case, the tube axis is aligned parallel to a solenoidal magnetic field of flux density B(T), and the electrons, emitted from the photocathode with transverse momentum mv (eV/c, Lambertian angular distribution), follow a helix of diameter $\phi(\mu m) = 2mv / B = 17.5$ µm for 1 T and 2.6 eV kinetic energy. This version is particularly suitable for so called delay tubes [42], where electrons that travel slowly to-and-fro (~1m/µs) achieve delays of about 1µs before a selected image can be gated by the first-level trigger of a detector for further data processing via the silicon pixel anode.

First experiments with an ISPA-tube have been performed recently by tracking cosmic muons [45] and 120 GeV/c negative pions [46] through 60 µm diameter scintillating fibres. The applied ISPA-tube[#7] encloses with its vacuum sealed cylinder of 45 mm length and 35 mm diameter, a photocathode viewed at 30 mm distance by a $8\ mm \times 4.8\ mm$ silicon chip containing 1024 pixels of $75\ \mu m \times 500\ \mu m$ edges. Each silicon pixel is bonded with Pb-Sn solder bumps to its proper electronic front-end channel. The electronics consist of preamplifier, comparator with adjustable threshold, delay line, coincidence logic and memory element [47, 48][#8] . The pixel response is binary and the 64 columns of 16 pixels are readout at 5 to 10 MHz frequency resulting in 6 to 12 µs readout time. The bump-bonding of the individual pixel electronics minimizes the noise and their line-parallel readout reduces the wire connections through the tube's envelope to 34 instead of more than thousand. The tracking results are reported in chapter IVe.

IV SCINTILLATING FIBRES IN HIGH ENERGY PHYSICS

1) Particle tracking

a) Basic considerations

Particle tracking, in particular at high luminosity colliders, requires fast response, good spatial precision, high two track resolution and fine granularity for good momentum resolution and small occupancy (the fraction of tracker cells occupied by particle hits). This fraction O is proportional to the collider luminosity L, the cross-section σ of

---

[#7] Assembled and manufactured by BV Delft Electronische Producten (DEP), NL-9300 AB Roden, The Netherlands. The chip was wire bonded at U.C.I. Microélectronique, F-91946 Les Ulis, France.

[#8] The CERN-ECP Microelectronics group designed the chip and supervised its manufacturing at different places : Canberra Semiconductor NV, B-2430 Olen, Belgium (silicon pixel array); GEC-Marconi Materials Technology Ltd, Caswell Towchester NN 128 EQ, United Kingdom (bump bonding); Smart Silicon System SA, CH-1012 Lausanne, Switzerland (electronics).

colliding particles, the number n per interaction of minimum bias particles per unit of rapidity η and the time t_b between two bunch crossings.

Apart from these collider parameters, we have also to take into account those of the tracker elements : their radial distance r from the collider axis, the rapidity range η_{max} covered, and their transverse cell dimensions s (e.g. fibre diameter) :

$$O = (L\sigma n t_b) \times \frac{s\ \eta_{max}}{2\ r\ \pi} \qquad (13)$$

In spite of lively development activities, direct applications of scintillating fibres as tracking devices in high energy physics experiments are still rare.

Apart from reducing the occupancy, fine granularity provides via high spatial resolution also excellent momentum resolution of the traced particles. The spatial resolution is composed of the spot size of individual hits and of the root-mean-square track residuals (spatial precision). The spot size is defined either by the pixel size of an ISPA tube (binary readout) or by the barycentres of several pixels (analog CCD-readout), or by drift clusters (gas filled detectors). The track residuals measure the displacements of spots (hits) from a fitted track.

The combined effect of spot size and track residuals defines the spatial resolution for a statistically meaningful sample in a Gaussian distribution, if the errors are calculated in a correct way. Its full width at half maximum (FWHM) indicates the two track resolution. For the momentum resolution we obtain finally [49] :

$$\left(\frac{\partial p}{p}\right)^2 = \left\{\left(\frac{G_c}{N}\right)^{1/2} \frac{\sigma}{L^2} \frac{p\ \sin\theta}{0.3B}\right\}_{curvature} + \left\{t^{1/2}\left(\frac{0.016\ \sin\theta}{0.3\ B\ L}\right)\right\}^2_{coul.\ scattering} \qquad (14)$$

with σ[m] meaning the spatial precision, B[T] the magnetic flux density, L[m] the track length, N the number of hits along the track, G a number which varies between 256 for optimum hit spacing (e.g. fibre shells) and 720 for continuous hit distribution (e.g. gas filled chambers) along L [50], θ the polar angle of the track and t the material layer in units of radiation lengths.

b) Sources of Noise in Particle Tracking

Noise, disturbing the clear appearance of particle tracks in readout patterns, can originate from different parts of the fibre set-up and its optoelectronic readout :

- from the fibres themselves, which can produce cross-talk and δ-rays generated by the traced particle.

- from photoelectron backscattering at the anodes of image intensifiers.

- from the electronic noise in the analog CCD-readout, which is not present in the binary readout of ISPA-tubes.

Cross-talk between fibres is caused by two different processes, one already described, is the transmission of scintillator light (e.g. p-terphenyl, table 3) across a small diameter fibre (radiative transitions) and its absorption in a neighbouring one by the wavelength shifter (e.g. POPOP, table 3). This can be avoided by doping the fibre with a 1-component scintillator (e.g. 3HF, PMP; table 3), which emits its light locally (~ 3 nm; Förster transitions).

The second source of cross-talk originates from the big fraction of untrapped scintillation light (approximately 90%). Although this fraction does not match the total reflection angle in order to be retrapped, it can reach the photocathode via scattering or diffusion if produced close to it. With fibre trackers (fig. 26) this noise can be neglected (fibre length $\geq$ 2 m), but it disturbs track reconstructions in short fibre targets [51]. This cross-talk can be strongly reduced with Extra Mural Absorbers (EMA) surrounding each fibre with a light absorbing or reflecting layer. For plastic fibre bundles such an EMA-protection for each individual fibre is not feasible. It can be partly replaced by an EMA at the bundle edges.

Photoelectrons are partly isotropically backscattered from the anodes of image intensifiers into the hemisphere towards the photocathode. Intensity coefficients for backscattering can be found for selected materials in ref. [27]. In many cases, the backscattered photoelectron carries away a considerable fraction of its initial energy, and its primary impact is therefore lost as a track signal. Since the accelerating electric field of the image intensifier turns the backscattered electron back towards the anode, it reappears as a noise hit. Without magnetic focussing the maximum displacement of this noise hit from its initial track position is twice the distance between cathode and anode. Therefore, most of the image frame is affected by this noise. This effect applies mainly to phosphor screen anodes. With digital readout from silicon pixels (ISPA-tubes [45, 46]) this noise is suppressed by appropriate threshold settings.

Typical CCD noise sources are: a) Photonic noise, which equals $\sqrt{N}$ (N being the number of electrons in a pixel) , b) Reset noise, which appears during charging the readout diode to its reference potential, c) Dark signals, which are generated by thermal excitation of electrons into the silicon conduction band. They double for every 10 degrees of temperature rise.

c) The UA2 Fibre Tracker

The first large size fibre tracking detector was studied, developed and built for the upgrade of the UA2 detector [52, 53] in collaboration between CERN and Saclay. The cylindrical fibre arrangement contained 60000 plastic fibres (polystyrene clad with polyvinyl acetate and doped with two components, PBD and POPOP, table 3). To avoid cross-talk, a thin aluminium layer was sputtered around each fibre. For stereo views, the

fibres were grouped into triplets, with one layer each running parallel to the detector axis and two layers placed at angles of ± 16° with respect to this axis. Details of the fibre tracker are shown in fig. 15. The eighteen actual tracking layers were followed by a tapered lead converter (1.5 rad. lengths) and six preshower fibre layers. In front of the tracking layers a Jet Vertex Detector, Silicon Hodoscope and Transition Radiation Detectors were placed. These devices introduced additional material in front of the fibre tracker and increased the probability of particle interactions and gamma conversions.

The fibre ends were bunched and coupled to 16 opto-electronic readout chains (fig. 16) placed at each detector end. Each chain consisted of two electrostatically focused image intensifiers and a proximity focussed one containing a micro channel plate (MCP). The images were transported subsequently via fibre optics windows, photocathodes and phosphor screens of the chain to CCDs, which provided finally the electronic signals for further data processing.

Alignment and intrinsic accuracy of the 1 mm fibres provided 0.4 mm track residuals. The two track resolution was about three fibre diameters. According to the material layers from other detectors in front of the fibres, there were roughly as many secondaries and conversions as primary tracks. Together with combinatoric overlaps this led to a serious ghost track problem.

d) The Chorus Fibre Tracker

A more recent application of fibre tracking is found in the Chorus experiment [54] which is designed to search for $\nu_\mu \rightarrow \nu_\tau$ neutrino oscillations in the CERN neutrino beam. The τ-decays will be detected in a 230 litre emulsion stack. To locate neutrino interactions in the emulsion targets, they are followed by flat rectangular fibre sheets, from which the tracks of secondaries are back-pointed to find the neutrino interaction coordinates in the emulsions.

There are more than 1 million fibres of 0.5 mm diameter installed having a total length of 2500 km. One of the opto-electronic read-out chains is shown in fig. 17. It consists of four image intensifiers including an image demagnification of 100:11, an MCP and a CCD of 550×228 pixels.

e) The Proposed Fine Grain Central Tracker

A different geometry [49, 55, 56] for particle tracking with scintillating fibres is found in the Fine Grain Central Tracker that uses three cylindrical fibre shells (fig. 18) of different radii with a common axis coinciding with that of the collider. There, the fibres will be arranged in four layers for each shell. Two layers (fig. 18) with fibres parallel to the shell (collider)-axis indicate the (r, φ)-coordinates. The two other layers u and v,

sandwiched between the two φ-layers, with oblique fibre directions, running at an angle of a few degrees with respect to the parallel ones, provide via their corresponding stereo view the z-coordinate of a particle track.

For all tracking arrangements, small diameter fibres are indispensable. Since fibres with diameters below 200 µm become difficult for individual handling and precise alignment, fused fibre bundles (fig. 7) were developed, which are strands of square cross-section with edge dimensions between 1 mm and a few millimetres and contain many hundreds of individual fibres with hexagonal shape and transverse dimensions corresponding to the requirements of the tracker design.

A major advantage of this fine grain tracking arrangement is that it produces several hits per fibre layer, according to the Poissonian probability of n hits within the path length t :

$$P_n = \frac{(ht)^n}{n!}\, e^{-ht} \qquad (15)$$

where h is the number of photons produced per mm fibre thickness in r-φ projection.

Typical ISPA-tracks are displayed in Fig. 19a. They were obtained with a 120 GeV/c negative pion beam [46], which traversed four fibre bundles (10 mm) glued together into a ribbon. Each bundle is of square cross-section with 2.5 mm edges (fig. 7) and contains 1600 coherently aligned hexagonal shaped scintillating fibres of 60 µm transverse dimensions (fig. 8), fused together by repeated drawing procedures. The magnetic focussed[#9] ISPA-tube was operated at 20 kV acceleration voltage across the 30 mm photocathode-anode gap. With 0.05 T magnetic flux density parallel to the electric field, the photoelectrons made one full helical turn until they hit after 30 mm distance the anode chip exactly opposite to their emission point. The oblong pixel dimensions (500 µm) were approximately aligned with the pion beam, whereas the 75 µm edges allow for spatial resolution perpendicular to the tracks.

Fig. 19b shows tracks from another fibre ribbon, where the two bundles u and v (with fibres oriented oblique to the pion beam by the angle α) are sandwiched between the bundles φ_1 and φ_2 running parallel to the beam. The symmetric stereo displacements u and v with respect to φ_1 and φ_2 provide the stereoview of the track and indicate the track distance d from the ISPA-tube : $d=(u+v)/2 \tan \alpha$. All tracks show the expected microvectors already assumed in ref. [49], rather than single hits (silicon microstrips, table 7) or clusters (microstrip gas chambers, table 7).

[#9] ISPA-tube prototypes with electrostatic or proximity focussing are also envisaged, depending on the applications considered.

The transverse hit distribution of 10^5 tracks is plotted in Fig. 20a. The Gaussian with a background level of ~1% shows a residual standard deviation σ of 42 µm, which corresponds to a two-track resolution (FWHM) of $2.4 \times \sigma$ = 100 µm. These values are mostly due to the binary readout of the 75 µm wide pixels, which does not indicate the number of hits within one pixel. An analog readout would reduce the dominant contribution of the pixel width and result in smaller residuals. This can be improved by producing anode chips with smaller pixel widths. The measured values for the centre-of-gravity precisions ε (Fig. 20b) and for the track directions (Fig. 20c) (which correspond to the precisions of the generated microvectors) are 15 µm and 8 mrad respectively[#10].

The symmetric microtracks of u - and v- layers can be paired (fig. 21) with respect to the φ-microtracks to form triplets, which finally indicate a real track. This advantage can be used for a new track recognition algorithm [57], which traces a particle from the outer layer to the inner one, following the φ and the u, v- sublayers. Comparison of Monte Carlo generated collider events with reconstructed ones [57] shows for only two fibre shells a reconstruction efficiency close to 100% with less than 1% ghost contribution. The average error on the reconstructed total momentum per event amounts to 6%.

f) Comparison of Fibres with other Tracking Media.

In the domain of particle tracking, scintillating fibres compete with other tracking media, mainly gas counters (in particular : microstrip gas chambers, MSGC [58-60]) and semiconductors (in particular : silicon strips and -pixels [55-56]). Some parameters of the three detector media, with respect to their application as tracking elements in the central detector region, are listed in table 7. These values are best estimates of the present state of detector performance. For valuable comparisons, the numbers given are normalized in the following way:

The number of hits is shown in units of 0.1 radiation length Xo. Heat production and the number of readout channels are indicated in units of subtended surface area [m^2] and hit thickness H, which means the layer of detector material required to achieve one readout signal (hit) from the energy loss of a minimum ionizing particle, (Si-detectors : 0.3 mm, MSGC : 2 mm, scint. fibres : 0.3 mm).

Spatial precision means the accuracy in locating a hit within the detector frame. The number listed for scintillating fibres represents the standard deviation (σ) of a Gaussian-shaped hit distribution [26, 43]. For silicon, most experimenters take either

---

[#10] The centre of gravity precision is related to the residual σ in fig. 20a via the number of hit pixels N: $\varepsilon = \sigma / \sqrt{N}$.

the sigma of the centroid (analog readout) or divide the shortest dimension of a detector element by $\sqrt{12}$ (binary readout) . For gas filled chambers, the spatial precision results from the accuracy with which the centroids of drift clusters can be located. In addition, for MSGCs there is a correlation between precision and detection efficiency. The single strip efficiency of 96% for perpendicular tracks decreases to between 35% and 15% for 30° angular deviation depending on the threshold [61]. This worsens precision and 2-track resolution accordingly.

For scintillating fibres, the two-track resolution is defined like the classical resolving power in optics, for separating two neighbouring objects (particle tracks), and the listed number refers therefore to the full width at half maximum (FWHM = 2.36 σ) of the Gaussian mentioned above [26, 43]. The two-track resolutions reported in most cases for silicon (Å 100 µm) and for perpendicular tracks in microstrip gas chambers (~300 µm) do not relate in the same way to their claimed precisions.

An important difference between fibres and the other media is in the readout. Every element (strip) of MSGCs and of silicon detectors (pixel or strip) needs a complete electronic readout chain. Fibres are read out at the end sections of their shell arrangements in parallel by optoelectronic tubes (ISPAs). Consequently, their number of channels is considerably reduced. This reflects also on the heat production, which represents a particular problem for semiconductors. It is caused by the leakage current of each detector element and by its electronics. A cautious estimate for semiconductors leads to about 1 mW per element.

2) Calorimetry with Scintillating Fibres

a) Basic considerations

A calorimeter measures the energy of incident electromagnetically or strongly interacting particles. Its energy resolution amounts to :

$$\frac{dE}{E} = \left(\frac{a^2}{E} + b^2 \right)^{\frac{1}{2}} \qquad (16)$$

where a is the energy dependent term. The constant term b describes the response of the calorimeter to electromagnetic (e) and to hadronic (h) interactions. Equal response (e/h=1) means a completely compensating calorimeter.

Normally, hadronic interactions terminate in nuclear breakups, where the nuclear binding energies (~ 20% of incident energy) will not contribute to the visible and measured energy. This can be compensated by employing uranium as radiator material where the fission processes increase the neutron component and make up for these losses [62]. In another approach plastic scintillators are employed as active sampling

material, because their hydrogen atoms respond better to the low energy neutron component of the hadronic cascade [63], and therefore enhance the hadronic response.

At the same time the calorimeter response to electromagnetic showers (mainly gammas from neutral pions which make about 30% of the incident energy) can be reduced by an appropriate fraction of high Z material (e.g. lead) which absorbs low energy photons before they reach the plastic sampling scintillator [64]. These requirements for a compensating calorimeter point to lead as energy absorber and to plastic scintillators as sampling material.

b) The Lead/Scintillating Fiber Calorimeter

These considerations and the requirement of fine grain energy sampling lead naturally to the Lead/Scintillating Fibre (Spaghetti) calorimeter. It is composed of 1 mm diameter scintillating fibres pointing at the colliders interaction region, which are interspersed in a lead matrix at 1:4 (plastic to lead) volume ratio. This geometry provides hermeticity and the different timing response for electromagnetic and hadronic interactions allows to combine the electromagnetic- and the hadronic calorimeters into one detector of about 2 m absorption thickness. This development has been initiated by Burmeister et. al. [65] with a lead-scintillating fibre sandwich geometry and was pursued by the LAA-project [66].

The electromagnetic energy resolution measured with a prototype of 41 modules [67] amounts to:

$$\frac{dE}{E} = \frac{14.4\%}{\sqrt{E(GeV)}} + 0.17\% \qquad (17a)$$

and the hadronic energy resolution, measured with a 155 module prototype of longitudinally unsegmented non-projective towers [68], is given by:

$$\frac{dE}{E} = \frac{28\%}{\sqrt{E(GeV)}} + 2.5\% \qquad (17b)$$

These modules are now used as a calorimeter in the WA-89 experiment behind the Omega-fixed target spectrometer at CERN.

The position resolution for incident electrons is [69]:

$$\sigma_x = \frac{5.0\ mm}{\sqrt{E(GeV)}} + 0.2\ mm \qquad (18a)$$

For single hadrons this resolution amounts to [70] :

$$\sigma = \frac{31.4\ mm}{\sqrt{E(GeV)}} \qquad (18b)$$

Several fibre calorimeters are already in use or are planned at different particle physics experiments. One of the earliest applications was with the electromagnetic calorimeter of the JETSET experiment [71] at the CERN Low Energy Antiproton Ring (LEAR). It is assembled of individual towers which point to the interaction region and form a hermetically sealed structure [72]. The design depth is 12.5 radiation lengths (0.2 m). A matrix of 1 mm polystyrene scintillating fibres is embedded in a lead-antimony alloy via an epoxy, which envelops the cladding of each fibre. The resulting volume ratio fibre: lead : epoxy amounts to 50 : 35 : 15. This layout is not intended to yield e/h-compensation but is optimized for electromagnetic energy resolution : $dE/E = 0.06/\sqrt{E}$.

The Chorus experiment [54] uses a longitudinally segmented fibre calorimeter with scintillating fibres running transverse to the neutrino beam. This allows for the insertion of limited streamer tubes to track penetrating muons. It consists of three sections : the first one of high granularity measures the electromagnetic component, and the two others with lower granularity the hadronic one. The volume ratio is four parts of lead to one part of plastic fibres.

A “spaghetti” type calorimeter is being built for the KLOE experiment [73] at the ϕ-factory DAPHNE in Frascati, Italy. In the 3.75 m long barrel region of 4 m outer diameter, the scintillating fibres run parallel to the collider beam. In the two endcaps, the fibre directions are orthogonal to the beam. The construction uses a glueing technique and the resulting fibre : lead : epoxy volume ratio is 48 : 42 : 10.

At the DESY electron-proton collider HERA the H1-experiment plans to build a fibre calorimeter to extend their large liquid argon calorimeter in the backward p-scattering region [74]. The electromagnetic section would contain 0.5 mm diameter scintillating fibres embedded in lead at a volume ratio of 2 (Pb) : 1. The hadronic part is planned for 1 mm diameter fibres with 4(Pb) : 1 volume ratio and will be one interaction length deep.

c) Comparison with other Calorimeter Techniques.

There are several competing methods for calorimetric energy measurements. Closely related to scintillating fibres are scintillating plates, interleaved with heavy material absorbers. A new development [75] is the calorimeter with scintillating tiles oriented radially to the collider axis. Each tile is coupled to a clear or wavelength-shifting read-out fibre. Simplicity of mechanical construction is purchased at the expense of coarse granularity and difficult tuning of complete compensation.

A completely different class of detectors is defined by liquid argon calorimeters containing absorber plates and electrodes for charge collection. The electron drift velocities of ~5 mm/μs produce long occupation times of 300 ns to 500 ns within the argon gaps between the plates. This drawback must be compensated by bipolar pulse-

shaping, which decreases the signal/noise ratio. An interesting arrangement is the accordion geometry [76], which provides very short cable connections from the charge collecting electrodes to the preamplifiers. They yield rise times of ~ 30 ns. The electromagnetic energy resolution achieved with an accordion calorimeter is similar to that of the spaghetti calorimeter with a tiny advantage of the accordion.

3) Dose Rates and Radiation Damage for Fibre Detectors at LHC

Minimum biased events produced as background from pp-collisions scale with luminosity, multiplicity and particle cross-section. They are by far the main source for the radiation dose around the crossing points of a hadron collider. The dose rate in Gy (Gray= 1 Joule Kg^{-1}) per year (Yr^{-1}) can be expressed in the following way :

$$D_0(r)\ [\mathrm{Gy\ yr^{-1}}] = \mathrm{const}\ \frac{dE}{dx}\ \frac{1}{\sin\theta}\ L \times \sigma_{inel} \times H \times \left(\pi\ r^2\right)^{-1} \sin\theta \qquad (19)$$

with $(dE/dx)\ (\sin\theta)^{-1}$ meaning the stopping power (LHC : 2 GeV cm^2 Kg^{-1}) for minimum ionizing particles emitted at the polar angle θ ($\cos\theta = \tanh\eta$, where η is the rapidity), L the luminosity [$10^{34} cm^{-2} s^{-1}$] of the collider, σ_{inel} [cm^2] the inelastic cross-section for pp collisions (LHC : 85 mb), H the number of particles per collision and per unit of rapidity (LHC : 6), r [cm] the distance from the collider axis and $H \sin\theta / \pi r^2$ is the number of particles per unit surface of a cylindrical detector. The term const [1.6×10^{-3} Joules GeV^{-1} yr^{-1}] contains the conversion from GeV into Joule ($1.6\ 10^{-10}$) and from seconds to year (10^7) if we assume a yearly operation of 10^7 s, which corresponds to about 115 days.

This relation changes if a solenoidal field with flux density B is applied in the tracking region [44] :

$$D_B(r) = D_0(r) \left\{ 2 < n_c > \int_{x_r}^{x_c} f(x')dx' + \int_{x_c}^{\infty} f(x')dx' \right\} \qquad (20)$$

where $<n_c> = \sinh\eta_{max}/\pi \sinh\eta$ [49] is the average number of particle curls in the rapidity range $0 < \eta < \eta_{max}$, $f(x) = x\ e^{-x}$ is the transverse momentum distribution of min. bias particles taken from Monte Carlo data, and $x = 2p_t / <p_t> = 0.3\ B\ r / <p_t>$. The average transverse momentum p_t of min. bias particles depends on the collider's centre-of-mass energy E_{cm} and can be approximated by :$<p_t> \sim 0.44 + 0.071 \log E_{cm}$.

Particles with curling diameters between zero and distance $r = p_t/0.15\ B$ from the collider axis do not contribute to the radiation dose, therefore the first integral of relation (20) spans between x_r and x_c, where c means the outer radius of the free barrel, with a calorimeter or a solenoid as boundary. The second integral covers the contribution due to those particles which are stopped curling by this boundary.

The annual dose rates for LHC are shown versus the distance from the collider axis in fig. 22. A solenoidal field of 4 T changes the dose rates for LHC as indicated in fig. 22 [44]. For the tracker scenario shown in fig. 18, this means maximum annual dose rates at 0.75 m distance of 0.45kGy (45 kRad), which is certainly tolerable for the scintillating fibres during several years of operation.

In general, radiation damage from ionizing radiation and from neutrons results in complex deteriorations of scintillating fibres : It causes optical colouration (colour centres) of the basic matrix (core), which decreases its light transmission ; it also can yield chemical degradation of the added scintillators, which reduces their light emission ; it can worsen the quality of cladding layers, which increases the reflection losses at their core-cladding interface ; together with the infiltration of gases, it may produce radicals, which change the chemical structure and affect the fibre performance.

The extent of damage in scintillating fibres is influenced by many parameters : dose rate [77], recovery [78, 79], ambient temperature [80], colouration of basic matrix [81, 82], chemical structure and molar fractions of added dopants [83, 84, 44], nature of surrounding gases [85, 86], etc. Therefore, it is difficult, to disentangle the different contributions to radiation damage of scintillating fibres. An exhaustive treatise of these effects would require a separate review.

It is already certain that high dose rates to which scintillators are exposed for tests, cause more damage than low ones. The dose rate of LHC at 10^{34} cm^{-2} s^{-1} luminosity would average only 3.9 Gy/day (fig. 22) at 0.75 m distance of the inner fibre shell (fig. 18). Even for long term irradiation tests, the applied rate is about 100 times higher, in order to achieve doses of several tens of kGy within a reasonable time (months).

As far as dopants are concerned, it has been clearly demonstrated [83, 84] that 3-hydroxyflavone (3HF) [21] doped fibres show smaller permanent radiation damage than those doped with other aromatic compounds. Fortunately, this dopant shows a large Stokes' shift and can be applied as a 1-component system (table 3) which emits around 530 nm. On the other hand, its fluorescence yield is only 0.4 (table 3), which makes it less suitable for particle tracking but is still more than adequate for calorimetric applications.

With LHC, neutron fluxes in calorimeters reach levels well above 10^{15} neutrons per cm^2 and year [87] at an integrated luminosity of 10^{41} cm^{-2} and 60 mbarns inelastic p-p cross-sections. Although the lead/fibre calorimeter yields the lowest neutron production (table 5 in ref. [87]), the radiation load on the fibres is important. Also the radiation level caused by gammas from neutral pion decay is considerable. Damage to the calorimeter's scintillating fibres from these processes would change the e/h-ratio and therefore worsen its energy resolution via the constant term b (relation 16). Also, all changes in uniformity of the fibres' light transmission, which could occur because of local radiation damage, would necessitate frequent recalibrations of the calorimeter.

Therefore, the RD-25 collaboration studied carefully the resistance of different fibre types with full length modules at a high intensity 0.5 GeV electron beam (CERN-LIL) [88]. Fig. 23 shows the added constant term (relation 16) as a function of incident electron energy after an exposure at LIL, which would correspond to 4 years LHC operation at 2.5 rapidity. The figure shows clearly the advantage of 3-HF doped fibres clad with fluorinated polymethacrylate.

V CONCLUSIONS

During the past few years the performance of scintillating fibres has improved considerably. Developments were mainly based on polystyrene cores and include the introduction of 1-component dopants (table 3 : PMP [19, 20], 3HF [21], etc) which prevent cross-talk for small diameter fibres [22]. For fibres with diameters below 100 µm fused bundles were developed [15], with high packing fractions [26] and excellent coherency for precise alignment in tracking arrangements. The fraction of trapped light has been improved by a factor of 1.75 [23] with fluorinated polymethacrylate cladding. In addition, general improvements on fibre production, which mainly reduced the light attenuation in the polystyrene cores and the reflection losses at the core-cladding interfaces, enhanced finally the number of photoelectrons / mm (hit densities). These improvements on fibre performance are illustrated in fig. 24 which shows the considerable differences in hit densities of 60 µm fibres contained in fused bundles between 1990 and 1993.

Recently, new readout techniques have been developed in two different ways, which both avoid the bulky opto-electronic chains of classical image intensifiers, where the scintillating light is transported via phosphor screens to CCD-readout. One, is the new development of Visible Light Photon Counters (VLPC), which are silicon solid state photomultipliers [28]. They need to be cryogenically cooled to 6.5 K and are coupled to the scintillating fibres via clear ones. They reach 0.85 quantum efficiency at 550 nm [29].

The second technique follows the development of hybrid photo photomultiplier tubes (HPMT, fig. 6) [30-37, 24, 25], which employ photocathodes to allow light detection from scintillating fibres for photoncounting. The high potential difference (> 10 keV) between photocathode and silicon anode enhances considerably the collection efficiency of electrons emitted from the photocathode, as compared to the Quantacon with 300 V to 500 V at the first dynode. Newest developments [45, 46] place a silicon pixel readout opposite and in proximity to the photocathode (ISPA-tube, fig. 13) to maintain the fibre granularity also for the electronic readout. ISPA-tubes replace in a cheaper and space saving way the classical optoelectronic chains with better spatial resolution and higher signal/noise ratios.

Until now, particle tracking with scintillating fibres has been mainly hampered by coarse fibre granularities and by the bulky opto-electronic readout chains. Fibre occupancy, resolution of particle momenta, and reconstruction efficiency of collider events [57] can be improved with thin shell arrangements of fine grain bundles aligned for stereoscopic views (fig. 18). These shells are distributed over the free barrel diameter bordered by the inner surface of the calorimeter or the solenoid of the detector. This arrangement results in large track lengths L (in fig. 18 : L= 1.25 m), which improve considerably the measurement of track curvature (L^2-dependence in relation 14), and increase the back-pointing accuracies to the collision vertices of hadron colliders. Each fibre bundle produces several hits (relation 15) and therefore

micro tracks of a few millimetres (fig. 19), rather than single hits or clusters as with silicon layers or MSGC-modules. Since all bundles are readout at the cylindric end-sections rather than at the shell surfaces, the number of readout channels is much lower than with competing silicon strips or pixels and MSGCs (table 7). Therefore, extra cooling loops, representing additional passive material to remove electronic heat are not needed for the fibre tracker.

In calorimetry, the volume fraction of scintillating fibres, distributed as sampling material in a lead absorber, can be precisely tuned to achieve full electron-hadron compensation. This improves the energy resolution of the calorimeter since the constant term in relation 16 becomes small. Another advantage is the fast signal response (~15 ns) due to the short decay time of the emitted fibre light (table 3). These response times are achieved without signal shaping, which would further shorten them by a significant factor. Electron/pion discrimination can be achieved with longitudinal shower sampling, effective shower time and/or lateral shower sampling. In combination, these selection criteria yield rejection of 10^3 within about 100 ns.

Acknowledgements

I thank C. D' Ambrosio, T. Gys, D. Puertolas for their critical comments and suggestions. I am grateful to R. W. Kenney (Lawrence Berkeley Laboratory), who, during his editing work, pointed out many potential improvements.

GLOSSARY

Absorption band : Wavelength region, where incident light is absorbed due to excitations of the electronic and the vibrational energy levels of chemical compounds.

Cladding : Thin (2 µm to 5 µm) material layer (mostly PMMA) surrounding the fibre core. Its refractive index is smaller than that of the fibre core, to enable total light reflections at the core-cladding interface.

Cross-talk : Light produced via particle ionisation in one fibre is transmitted into neighbouring fibres due to radiative exchange between scintillator and wavelength-shifter (2-component systems, table 3). The absorption length of the emitted scintillation light exceeeds the fibre diameter and excites the wavelength shifter in a neighbouring fibre. This phenomenon can be avoided either by a 1-component dopant (e.g. PMP, 3HF, table 3) or by surrounding each fibre with an EMA-coating.

Extra mural absorber (EMA) : Light absorbing or reflecting coatings which surround each fibre to suppress cross-talk between neighbouring fibres. For fused plastic fibre bundles it is not possible to coat each individual fibre with EMA (as it is with glass fibre bundles). Therefore, it is imperative to dope them with 1-component scintillators (table 3) at concentrations, which allow for local Förster transitions to avoid cross-talk.

Extinction coefficient (decadic molar) $\varepsilon(\lambda)$: Transformation of recorded light intensities (I) after transmission of incident light (I_0) through absorbing media :

$$\varepsilon(\lambda) = -0.4343 \ln(I / I_0) / C \times d \qquad [\text{l mole}^{-1}\ \text{cm}^{-1}]$$

with C meaning the molar concentration of the absorber and d the absorption thickness.

Fibre bundle : Small diameter fibres fused coherently together during the drawing process. The bundles are of square or hexagonal outer cross-sections with edge lengths greater than 1 mm. They contain several hundreds of individual fibres. Their cross-sections are hexagonal due to the energy minimum required for this configuration. They are separated from each other by thin cladding layers.

Fibre optics window : clad glass fibres of 5 µm to 20 µm diameter are fused together to serve as vacuum tight windows (thickness > 5 mm) for photocathodes and phosphor screens. They are indispensable, if spatial resolution of fibres must be conserved. To avoid light losses, their numerical aperture (NA) must be greater than that of scintillating fibres.

Förster transitions : Radiationless energy transitions between donor molecules (e.g. polysteyrene) and acceptor (scintillator) molecules (in contrast to radiative energy transfer). They require small distances (0.5 nm to 3 nm) between donors and acceptors, which requires molar scintillator concentrations (above 0.02 molar fraction), at which, on the average, one scintillator molecule is inside a sphere with a radius corresponding to these distances.

Förster transitions provide local light emission (in contrast to radiative ones) and therefore avoid cross-talk between fibres of small diameters (fig. 5). Since they require high scintillator concentrations they can be achieved only with 1-component dopants, which have no (e.g. 3HF) or only small (e.g. PMP) overlaps between their absorption and emission bands (large Stokes'shift).

Förster [18] calculated critical distances between donor- and acceptor molecules, if there is sufficient overlap between the emission band of the donor and the absorption band of the acceptor. An extensive list of computed critical distances and molar concentrations can be found in ref. [89].

Hybrid Photomultiplier Tube (HPMT) : Electrons, emitted from a light detecting photocathode, are accelerated by a potential difference (^{3} 10 kV) towards a silicon diode. With low capacitances of the diode, the preamplifier input, and the connecting cables, it is possible to resolve energy peaks corresponding to up to 15 photoelectrons.

Magnetic flux density B : is measured in Tesla (1 T= 1 V s m^{-2}). The old unit is Gauss [G] : 1 G = 10^{-4} T. It is connected to the magnetic field strength H [A m^{-1}] via $B = \mu\ \mu_0\ H$, with μ_0 [V s A^{-1} m^{-1}] meaning the permeability of free space and μ [dimensionless] the permeability of the material present in the magnetic field.

The Lorentz force F between a particle of charge q and velocity v in a magnetic field amounts to : $\mathbf{F} = q\ (\mathbf{v} \times \mathbf{B})$. From this, the curling radius r of a charged particle with mass m in a solenoidal field is deduced : $r = m\ v\ /\ (q\ B)$ with $v \perp B$.

Microstrip gas chambers (MSGC) : Anode strips of 5 µm to 10 µm width and 50 µm wide parallel field strips are deposited via UV-lithography or plasma etching on substrates of high ohmic resistance. They form detector elements of about 200 µm pitch and 2 mm gas depth (cathode distance) for the development of electron avalanches.

Polymethylmethacrylate (PMMA) :

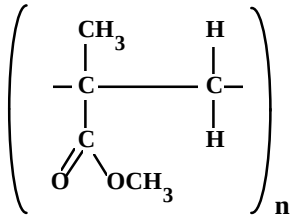

Cladding material of plastic step-fibres with 1.49 (590 nm) refractive index. The refractive index is reduced to 1.42, if fluorinated polymethacrylate is used as cladding material. This increases the trapping fraction by a factor 1.75.

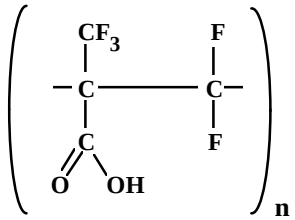

Polystyrene (PS) :

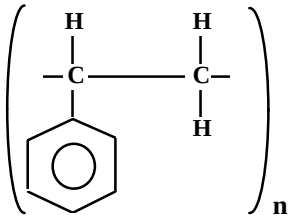

forms the basic structure of a fibre core. Its low fluorescence yield (0.03) must be enhanced by a scintillator.

Radiation dose : Absorbed ionization energy (Joule) per mass unit (kg) quoted in Gray ; 1 Gy = 1 J kg^{-1}. This unit is equivalent to the old unit Rad ;1 Rad = 10^{-2} Gy.

Scintillators : Aromatic compounds added to the styrene monomer (~ 0.02 molar fraction) of the fibre core for combined polymerisation. Scintillators enhance the poor fluorescence yield (0.03) of PS and provide Förster transitions.

The following two scintillators emit in the opaque wavelength region of polystyrene. Therefore, a wavelength shifter is needed (2-component system, table 3) to obtain an emission band in the transparent region of polystyrene (> 400 nm).

p-terphenyl :

PBD : 2-phenyl-5-(4-biphenylyl)-1,3,4-oxadiazole

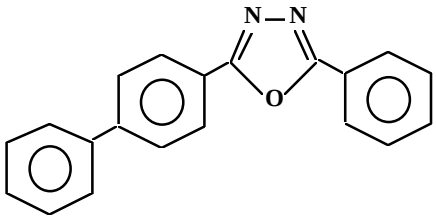

The following six scintillators emit in the transparent wavelength region of PS (1-component system, table 3), and do not need a wavelength shifter:

3HF : 3 hydroxyflavone

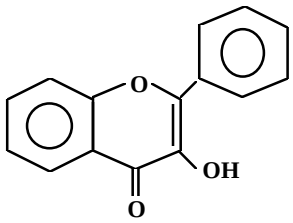

PMP 420 : 1-phenyl-3-mesityl-2-pyrazoline

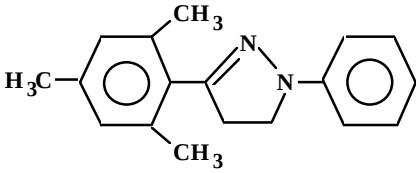

PMP 450 : 1-p-anisyl-3-mesityl-2-pyrazoline

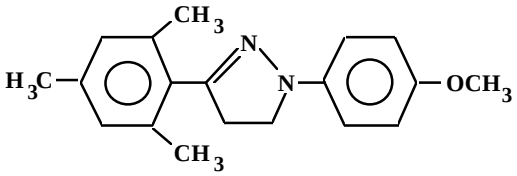

PBBO : 5 (1 naphthyl)-2 biphenyl-oxazole

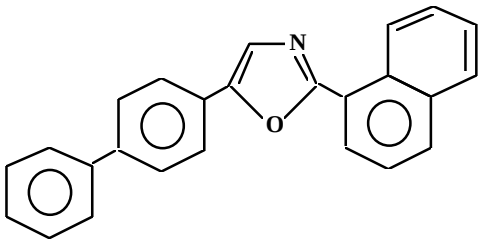

R39, R45 : Composition and structure unknown.

Silicon strips and pixels : are operated as diodes with reverse bias voltage. Electrons and holes, induced by ionizing particles, drift in a bias field of ~ 300 V mm^{-1} across a depletion layer of typically 0.3 mm thickness. Detector elements are geometrically arranged as single or double sided strips with 25 µm to 100 µm pitch. Their lengths of

several centimetres are limited by increasing capacitance. For two-dimensional readout, they are arranged as square or rectangular pixels with edges longer than 50 μm. All strips or pixels are wire- or bump-bonded, if not monolithically integrated to their individual front-end electronics.

Spatial frequency : means the number of line pairs per mm. The spatial frequency at which the MTF equals 0.03 represents the limiting resolution of an opto-electronic element. This number is often quoted by manufacturers of image intensifiers, fibre optics windows, etc.

Stokes' shift : Difference between the wavelengths of the absorption (λ_A)- and emission (λ_E)-maxima : $\lambda_A^{-1} - \lambda_E^{-1}$ [cm^{-1}] or $hc\,(\lambda_A^{-1} - \lambda_E^{-1})$ [eV].

Wavelength shifters : They form together with a scintillator (mostly p-terphenyl, which emits in the opaque wavelength region of polystyrene), a 2-component system (table 3). Their absorption bands overlap the scintillator's emission and their emission bands are in the transparent polystyrene region above 400 nm. Since their emission overlaps significantly their absorption band (small Stokes' shift, fig. 3c), they can be added to the styrene-monomer only in small molar fractions (< 0.002). This results in radiative (non-local) energy transfer between scintillator and wavelength shifter and therefore produces cross-talk between fibres of small diameter (fig. 5).

POPOP : p-bis [2-(5-phenyl oxazolyl)] benzene

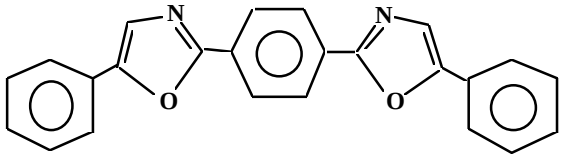

BBOT : 2,5-bis [5-tert-butylbenzoxazolyl (2)] thiophene

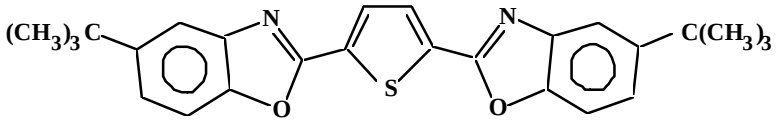

BDB :

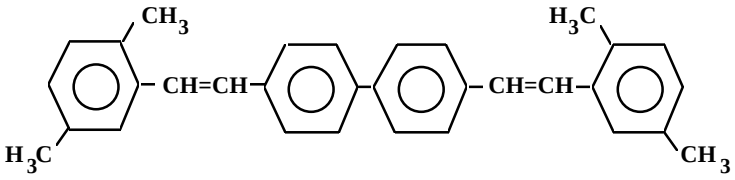

TPBD : 1,1,4,4-Tetraphenylbutadiene

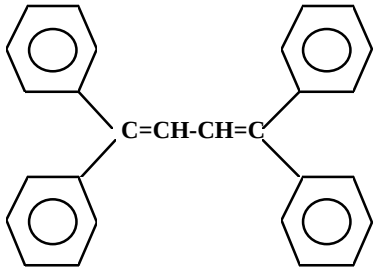

REFERENCES :

1 G. T. Reynolds and P.E. Condon ; *Rev. Sci. Instr*., 28 (1957) 1098.
2 R. J. Potter and R. E. Hopkins, *IRE Trans*., NS-7 (1960) 150.
3 L. Reiffel and N.S. Kappany, *Rev. Sci. Instr*., 31 (1960) 1136.
4 L. W. Jones and M. L. Perl, *Nuclear Instruments and Methods* 10 (1961) 348.
5 S. R. Borenstein et. al., *IEEE Transactions on Nuclear Science*, NS-29 (1982), 402.
6 L. R. Allemand et. al., *Nuclear Instruments and Methods* 225 (1984) 522.
7 H. Blumenfeld et. al., *Nuclear Instruments and Methods* 225 (1984) 518.
8 D. M. Potter et. al., *IEEE Transactions on Nuclear Science*, NS-29 (1982) 421.
9 R. Ruchti et. al. , *IEEE Transactions on Nuclear Science*, NS-30 (1983), 40.
10 A. Bross, *Nuclear Instruments and Methods* A247 (1986) 319.
11 A. Artamonov et. al., *Nuclear Instruments and Methods* A300 (1990) 53.
12 J. Bähr et. al. , *Nuclear Instruments and Methods* A306 (1991) 169.
13 C. Cianfarini et. al., CERN-PPE/93-135 (1993).
14 M. Atkinson et. al. , *Nuclear Instruments and Methods* A254 (1987) 500.
15 C. D'Ambrosio et. al., *Nuclear Instruments and Methods* A306 (1991) 549.
16 C. Angelini et. al., *Nuclear Instruments and Methods* A295 (1990) 299.
17 C. Angelini et. al., *Nuclear Instruments and Methods* A281 (1989) 50.
18 T. Förster, *Ann. Phys.* , 2 (1948) 55, and Discussions Faraday Soc. 27(1959)7.
19 H. Güsten et. al. , *J. Phys. Chem.* 82 (1978) 459.
20 C. D'Ambrosio et. al., *Appl. Spectroscopy* 45 (1991) 484.
21 C. L. Renschler and L. A. Harrah, *Nuclear Instruments and Methods* A235 (1985) 41.
22 C. D'Ambrosio et. al. "Scintillating Fibres for Central Tracking of Charged Particles", in : "New Technologies for Supercolliders" edited by L. Cifarelli and T. Ypsilantis, Plenum Publishing Corp. (1991), New York.
23 C. D'Ambrosio et. al., *Nuclear Instruments and Methods* A332 (1993) 134.

24 C. D'Ambrosio et. al., *Nuclear Instruments and Methods* A338 (1994) 389.
25 C. D'Ambrosio et. al., *Nuclear Instruments and Methods* A345 (1994) 279.
26 C. D'Ambrosio et. al., *Nuclear Instruments and Methods* A325 (1993) 161.
27 E. H. Darlington, *J. Phys.*, D 8 (1975) 85.
28 M. D. Petroff and W. G. Stapelbroek, *IEEE Trans. on Nucl. Sci.* NS-36, (1989), 158.
29 M. Atac et. al. , *Nuclear Instruments and Methods* A314 (1992) 56.
30 F.S. Goulding, *IEEE Transactions on Nuclear Science*, NS-11, (1964), 177.
31 R. Kalibjian, *IEEE Transactions on Nuclear Science*, NS-12 (1965), 367.
32 J.M. Abraham, L.G. Wolfgang and C.N. Inskeep, *Advances in Electronics and Electron Physics*, (1966), 671.
33 J.M. Abraham, L.G. Wolfgang and C.N. Inskeep, *IEEE Transactions on Nuclear Science*, NS-13, (1966), 46.
34 R. Kalibjian, *IEEE Transactions on Nuclear Science*, NS-13, (1966), 54.
35 P. Chevalier, *Nuclear Instruments and Methods* , 50, (1967), 346.
36 J. Fertin, B. Lach, J. Meuleman, J. Dupuis, L. Hermite and R. Petit, *IEEE Transactions on Nuclear Science*, NS-15, (1968), 179.
37 E.A. Beaver, C.E. McIlwain, J.P. Choisser and W. Wysoczanski, *Advances in Electronics and Electron Physics*, 33B, 5th Symposium on Photoelectronic Image Devices, (1972), 863.
38 R. DeSalvo, W. Hao, K. You, Y. Wang and C. Xu, *Nuclear Instruments and Methods* , A315 (1992), 375.
39 D. Autiero et. al., INFN PI/AE 05/95 Pisa, Italy, submitted to *Nuclear Instruments and Methods* .
40 G. Anzivino et. al. : "Failure Modes of Large Surface Avalanche Photodiodes in High Energy Physics Environments". Proceedings of the IV Intern. Conf. on Calorimetry in High Energy Physics, Elba, Italy, Sept. 1993.
41 W. Brückner et. al., *Nuclear Instruments and Methods* A313 (1992) 429.
42 T. Gys et al., in "New Technologies for Supercolliders", Proceedings of the 12th Workshop of the INFN ELOISATRON Project, Ettore Maiorana Centre for Scientific Culture, Erice, Italy, September 15-20 1990, Eds L. Cifarelli and T. Ypsilantis, Plenum Press 1991.
43 C. D'Ambrosio et al., in Proceedings of the "Joint International Lepton-Photon Symposium & Europhysics conference on High Energy Physics" Geneva, Switzerland 25 July - 1 August 1991, Eds S. Hegarty, K. Potter and E. Quercigh, World Scientific 1992.
44 RD-7 Status Report, CERN/DRDC 93-42 (1993).
45 T. Gys et. al., *Nuclear Instruments and Methods,* A355 (1995) 386.
46 C. D'Ambrosio et. al., *Nuclear Instruments and Methods,* A359 (1995) 618.
47 F. Anghinolfi et. al. , IEE Trans. Nucl. Sci. NS-39 (1992) 654.
48 E. H. M. Heijne et. al., *Nuclear Instruments and Methods,* A349 (1994) 138.
49 C. D'Ambrosio et. al., *Nuclear Instruments and Methods* A322 (1992) 20.
50 R.L. Gluckstern, *Nuclear Instruments and Methods* 24 (1963) 381.
51 C. Angelini et. al., *Nuclear Instruments and Methods* A289 (1990) 356.
52 J. Alitti et. al., *Nuclear Instruments and Methods* A273 (1988) 135.
53 R. E. Ansorge et. al., *Nuclear Instruments and Methods* A265 (1988) 33.

54 Chorus Collaboration, CERN-PPE/93-131.
55 CMS– Letter of Intent, CERN/LHCC 92-3 (1992).
56 ATLAS– Letter of Intent, CERN/LHCC 92-4 (1992).
57 F. Anselmo et. al., *Nuclear Instruments and Methods* A349 (1994) 398.
58 A. Oed, *Nuclear Instruments and Methods* A263 (1988) 351.
59 F. Angelini et. al. , *Nuclear Instruments and Methods* A283 (1989) 755.
60 F. Udo, Proc. of the Large Hadron Collider Workshop, eds. G. Jarlskog and D. Rein, CERN 90-10, Vol. 3 (1990), p. 219.
61 RD-28 Status Report, CERN/DRDC 93-34 (1993).
62 C. W. Fabjan et. al. , *Nuclear Instruments and Methods* 141 (1977) 61.
63 J. Brau and T. A. Gabriel, *Nuclear Instruments and Methods* A238 (1985) 489.
64 E. Bernardi et. al. , *Nuclear Instruments and Methods* A262 (1987) 229.
65 H. Burmeister et. al., *Nuclear Instruments and Methods* 225 (1984) 530.
66 A. Zichichi : " The LAA-project", *ICFA Instrum. Bull.* , 3 (1987) 17.
67 G. Anzivino et. al. : "Results on a fully projective lead/scintillating fibre. calorimeter". Proceedings of the IV Intern. Conf. on Calorimetry in High Energy Physics, Elba, Italy, Sept. 1993.
68 D. Acosta et. al. , *Nuclear Instruments and Methods* A308 (1991) 481.
69 B. Bencheickh et. al. , *Nuclear Instruments and Methods* A315 (1992) 354.
70 D. Acosta et. al. , *Nuclear Instruments and Methods* A305 (1991) 55.
71 JETSET collaboration PS202 CERN/PSCC 86-23 (1986)
72 D. W. Hertzog et. al. , *Nuclear Instruments and Methods* A294 (1990) 446.
73 Technical Proposal of the KLOE-collaboration : LNF 93/002 (1993) IR.
74 Technical Proposal of the H1-collaboration DESY PRC 93/02 (1993).
75 M. Bosman et. al., CERN/DRDC 93-3 (1993).
76 B. Aubert et. al., *Nuclear Instruments and Methods* A321 (1992) 467.
77 K. Wick et. al. , *Nuclear Instruments and Methods* A271 (1988) 701.
78 V. D. Bezuglii and L. L. Nagormaya , J. Nucl. Eng. 19 (1965) 1182.
79 G. Oldham and A. R. Ware, Rad. Eff. , 26 (1975) 95.
80 C. Zorn et. al. , *Nuclear Instruments and Methods* A276 (1989) 58.
81 H. Schönbacher and W. Witzeling, *Nuclear Instruments and Methods* 165 (1979) 517.
82 K. F. Johnson et. al. , IEEE Trans. Nucl. Sci. , NS-37 (1990), 500.
83 C. Zorn et. al., *Nuclear Instruments and Methods* A273 (1988) 108.
84 S. Majewski et. al. , *Nuclear Instruments and Methods* A281 (1989) 500.
85 C. Zorn et. al., IEEE Trans. Nucl. Sci. , NS-36 (1989) 557.
86 C. Zorn et. al., IEEE Trans. Nucl. Sci. , NS-37 (1990) 504.
87 G. R. Stevenson, Proceedings of the ECFA-LHC-workshop, Aachen, Germany, CERN 90-10, Vol. III. p. 566.
88 G. Anzivino et. al. , *Radiat. Phys. and Chem.*, 41 (1992) 283.
89 I. B. Berlman, "Energy Transfer Parameters of Aromatic Compounds ", Academic Press, New York and London (1973)

Figure captions

Fig. 1 : Light cone injected with a numerical aperture NAi and passing through a step-index fibre under the total reflection angle α

Fig. 2 : Light attenuation measured at CERN by the RD-7 collaboration.

Fig. 3 : Absorption- and emission bands of the PS-fibre core (a), the p-terphenyl scintillator (b). The wavelength shifter POPOP (c) matches with its absorption band the p-terphenyl emission. The PMP 420 scintillator (d) spans due to its large Stokes' shift directly the wavelengths between the PS-emission and the transparent PS-region without needing a wavelength shifter.

Fig. 4 : Distortions of the short-wavelength flank of a 0.025 molar PMP 420 solution in toluene caused by different absorption paths of the same solution compared with a 0.0025 molar POPOP solution. The POPOP concentration had to be 10 times lower, because of its strong self-absorption in the overlap region.

Fig. 5 : Cross-talk of scintillating fibres (left hand) in a fibre bundle doped with p-terphenyl and POPOP (2-components). No cross-talk (right hand) in a fibre bundle with PMP doping (1-component), otherwise same excitation and light detection as for the left hand picture. The higher light output of the right hand monolayer also indicates that no scintillating light crosses to the neighbouring fibre layer.

Fig. 6 : The hybrid photomultiplier tube (HPMT).

Fig. 7 : Square bundle with 2.5 mm edge length. It contains about 1600 individual fibres of 60 µm diameter. The photograph is taken with a CCD-camera through 2 m bundle length.

Fig. 8 : An individual fibre within a bundle (fig. 7) surrounded by its six adjacent neighbours. It was illuminated at one end through a microscope objective and photographed at the other end after re-magnification with a CCD-camera.

Fig. 9 : Photoelectron distributions at different β-source distances measured with HPMT, and 60 µm dia. fibres.

Fig. 10 : Pulse height spectra [29] obtained at the indicated β-source positions. They include 3 m of clear fibres that guided the light from the 830 µm dia scintillating fibre to the He-Dewar that housed the VLPC at 6.5 K.

Fig. 11 : Proximity focussed image intensifier.
a : optics fibre window with photocathode ;
b : phosphor screen with optics fibre window.

Fig. 12 : Image intensifier multi-channel plate (MCP) configurations.

Fig. 13 : Image intensifier with silicon pixel arrays (proximity focussed ISPA-tube).

Fig. 14 : Silicon pixel readout organisation in a line-parallel mode for an ISPA-tube.

Fig. 15 : Vertical cut of the UA2 scintillating fibre detector.

Fig. 16 : An opto-electronic readout-chain of the UA2 fibre tracker. A: photocathodes; C: phosphor anodes; II: image intensifiers.

Fig. 17 : A chain of four image intensifiers ending with a CCD electronic readout for the Chorus scintillating fibre tracker.

Fig. 18 : Arrangement of scintillating fibre shells for tracking within the free barrel region of the calorimeter. r-φ plane seen at z=0. The magnified parts show the subdivision into the straight φ and the oblique u and v layers. The symmetric angles Δφ indicate the z coordinate via the indicated relation.

Fig. 19 : a) Typical track pattern from a 120 GeV/c negative pion beam traversing a 10 mm ribbon, with 60 µm diameter of scintillating fibres. The active frame size of the silicon chip is 4 mm x 7 mm (along the beam). The pixel size is 75 µm x 500 µm (along the beam.

b) Track pattern obtained with a stereoscopic bundle arrangement. The bundles u and v run with an angle $\pm\alpha = 7$ mrad oblique to the bundles φ_1 and φ_2. The beam passes straight through all four bundles and the ribbon end-face confronts the photocathode. There, its microvectors indicate the track distance from the photocathode: $d = (u+v) / 2\mathrm{tg}\alpha$. Note that the bundles φ_1 and φ_2 are

only partly covered by the active chip frame (dashed area) and that the pixel lengths (500 µm) do not exactly coincide with the bundle edges. The stereo angle is about ten times smaller than in ref. [49, 57] in order to match the bundles u and v with the active chip frame.

Fig. 20 : a) Residuals from 10^5 beam tracks (circles) and their Gaussian fit. The values for the standard deviations σ and full widths at half maximum (FWHM) are due to the binary readout, which does not indicate the number of hits within one pixel. An analog readout would reduce the dominant contribution of the 75 µm pixel width and improve σ and FWHM.

b) Measured centre-of-gravity precision ε. It is related to the residuals σ of Fig. a) via the number of hit pixels N: $\varepsilon = \sigma / \sqrt{N}$. The asymmetric shape is mainly due to the diminishing number of hit pixels at the right-hand part.

c) Measured direction precisions of 10^5 accumulated tracks. They indicate the accuracy with which the microvectors of a tracker plane or shell [57] can be projected to the next plane or shell.

Fig. 21 : a) A typical microtrack triplet from a particle passing through a tracker shell. The track segments in the u- and v- layers are shifted by $\Delta\varphi$ in increasing and decreasing azimuth angle φ. The shift $\Delta\varphi$ corresponds to the z-coordinate of the track (fig. 18).

b) The resulting track segment after shifting the u- and v- microtracks by $\pm \Delta\varphi$.

Fig. 22 : Annual dose at the inner detector cavity within ± 3 rapidity for the indicated decadic luminosities. At 4 T, the particles curl with ~ 1 m max. radius. The unit Gray (Gy) equals 1 Joule/kg or 100 Rad.

Fig. 23 : Monte Carlo results on the additional constant term in the electromagnetic energy resolution for the measured radiation hardness of 3HF (500 ppm) fibres with radiation hard cladding (black dots) and for SCSF81 Y9 fibres with standard cladding (white dots), as a function of the incident electron energy (Spaghetti calorimeter [88]).

Fig. 24 : Improvements on hit densities (photoelectrons/mm) for fibre bundles, containing 60 µm fibres, during the last years. The main progress is due to higher trapping fractions from fluorinated cladding, better collection efficiencies of photoelectrons from the HPMT-photocathodes and improved manufacturing procedures.